



# Peculiarities of Si and SiO<sub>2</sub> Etching Kinetics in HBr + Cl<sub>2</sub> + O<sub>2</sub> Inductively Coupled Plasma

Byung Jun Lee<sup>1</sup> · Alexander Efremov<sup>2</sup> · Jihun Kim<sup>1</sup> · Changmok Kim<sup>1</sup> · Kwang-Ho Kwon<sup>1</sup>

Received: 7 March 2018 / Accepted: 1 November 2018 / Published online: 10 November 2018  
© Springer Science+Business Media, LLC, part of Springer Nature 2018

## Abstract

Peculiarities of the etching kinetics and mechanisms for Si and SiO<sub>2</sub> in the HBr + Cl<sub>2</sub> + O<sub>2</sub> inductively coupled plasma were investigated by analyzing the relationships between etching rates and fluxes of active species. The data on plasma parameters, plasma chemistry, and the steady-state plasma composition were obtained using both Langmuir probe diagnostics and 0-dimensional plasma modeling. It was found that an increase in the Cl<sub>2</sub> mixing ratio and input power causes similar trends in the changes in ion energy flux and halogen atom flux but results in different tendencies for both Si and SiO<sub>2</sub> etching rates. It was shown that the influence of input process parameters (HBr/Cl<sub>2</sub> mixing ratio, input power, and bias power) on the Si and SiO<sub>2</sub> etching kinetics may be adequately described in terms of the oxygen atom flux-sensitive reaction probability. The latter directly correlates with the oxygen atom flux/ion energy flux ratio.

**Keywords** Si and SiO<sub>2</sub> etching rates · Halogen atom flux · Ion energy flux · Oxygen atom flux · Effective reaction probability

## Introduction

Silicon and silicon-based compounds (SiO<sub>2</sub>, Si<sub>3</sub>N<sub>4</sub>, and SiC) are the basis of modern electronic device technology being used as the wafer materials, hard masks, and semiconductor and dielectric layers [1–3]. As most of the applications require precision patterning of the material surface, the development of a dry etching process for both Si and SiO<sub>2</sub> is an important task to be solved for advanced micro- and nano-device characteristics. From Refs. [2–5], one can conclude that the principal requirements for advanced Si etching technology are: (1) a reasonably high etching rate; (2) a sufficiently high etching selectivity with respect to both mask and under-layered materials; and (3) an anisotropic etching that

---

✉ Kwang-Ho Kwon  
kwonkh@korea.ac.kr

<sup>1</sup> Department of Control and Instrumentation Engineering, Korea University, Sejong 339-700, South Korea

<sup>2</sup> Department of Electronic Devices and Materials Technology, State University of Chemistry and Technology, 7 Sheremetevsky av., Ivanovo, Russia 153000

results in minimum erosion of the sidewalls. An optimal combination of the above features requires an accurate control of output process characteristics and an ability to adjust contributions of physical (physical sputtering, ion-assisted chemical reaction in ion-flux-limited mode) and chemical (spontaneous chemical reaction, ion-assisted chemical reaction in neutral-flux-limited mode) etching pathways. As such, interconnections between the adjustable process parameters, plasma chemistry, and etching kinetics must be clearly understood for the given combination of gas system and etched material.

Until now, a considerable number of experimental and theoretical (with using of various models for gas-phase and heterogeneous processes) works have dealt with etching characteristics and mechanisms for both Si and SiO<sub>2</sub> in fluorine-based gas chemistries [1–3, 5]. Accordingly, the results of these works have provided detailed data on the relationships between input process conditions (pressure, input power, and bias power), plasma parameters, and the heterogeneous stages of the etching process, including both etching and polymerization effects. It was also shown that the major disadvantage of all fluorine-based gas chemistries is the low etching anisotropy of Si due to an effective spontaneous reaction between silicon and fluorine atoms. Such a situation results from the low size of F atoms, which allows one to penetrate easily into the lattice and form the highly volatile SiF<sub>4</sub>. This problem may be solved by using chlorine- and bromine-based gas chemistry, and namely the Cl<sub>2</sub>- and HBr-containing gas mixtures [6, 7].

Currently, several studies have reported on the plasma-assisted etching characteristics for Si and SiO<sub>2</sub> in HBr- [7–15] and Cl<sub>2</sub>-based [7–12, 16–18] chemistries. The most important results can be summarized as follows:

- The probability of spontaneous chemical reaction between halogen atoms and Si decreases in the sequence of F–Cl–Br [8, 13, 16]. This is probably due to increasing effective atom sizes that make it difficult for the larger atoms to penetrate the Si lattice. The spontaneous etching of SiO<sub>2</sub> by both Cl and Br atoms at typical process temperatures is thermodynamically forbidden and thus, appears to be negligible [5, 6]. As a result: (1) the exposure of the Si surface to Cl or Br atoms leads to the formation of non-saturated low-volatile SiCl<sub>x</sub> or SiBr<sub>x</sub> compounds, while the rest of the Si–Si bonds remain in their original states [5, 13]; and (2) the steady-state chemical reaction of Si and SiO<sub>2</sub> with Cl and Br atoms requires ion bombardment of the etched surface [8, 16].
- Si and SiO<sub>2</sub> etching rates in HBr plasma are lower than those in Cl<sub>2</sub> plasma [8, 11]. This finding is in agreement with differences in volume densities and fluxes of halogen atoms in these gas systems [9, 19, 20]. At the same time, the HBr plasma allows one to obtain a higher etching selectivity with respect to the photoresist mask (due to the passivation of the photoresist surface by the UV irradiation [21, 22]) and provides a more anisotropic etching. The last feature is probably due to the lower neutral/charged ratio provided by the higher ion current density [23, 24] as well as the lower etching yield for Br atoms on the side walls because of the smaller angular scattering of heavier ions.
- The addition of oxygen to both HBr and Cl<sub>2</sub> lowers the Si and SiO<sub>2</sub> etching rates, but results in more anisotropic etching [10, 15, 18]. This effect is attributed to the formation of lower volatile SiO<sub>x</sub>Br<sub>y</sub> and SiO<sub>x</sub>Cl<sub>y</sub> compounds that passivate the sidewalls.

A deeper study of these works reveals important issues that require mandatory attention. First, most studies are of a purely experimental nature and discuss the etching kinetic and mechanisms only through the relationships between input process conditions, measured etching rates, and composition of reaction products. As a result, the existing data on the heterogeneous stages of the etching process are not matched with the changes in the

gas-phase plasma characteristics. Obviously, such a situation does not allow for an understanding of the entire process pathway and, thus, limits the possibility of optimizing the etching process. Furthermore, the studies did not consider the gas-phase plasma chemistry in the three-component  $\text{HBr} + \text{Cl}_2 + \text{O}_2$  gas mixture. For these reasons, questions related to steady-state plasma parameters, chemical reaction kinetics, and gas-phase composition were not explored in sufficient detail. At the same time, the  $\text{HBr} + \text{Cl}_2 + \text{O}_2$  gas system may exhibit the positive features of both bromine- and chlorine-based gas chemistries and provide some specific effects that are due to changes in plasma parameters and densities of plasma active species.

In this work, we attempted to combine the experimental and model-based approaches to analyze Si and  $\text{SiO}_2$  etching kinetics in  $\text{HBr} + \text{Cl}_2 + \text{O}_2$  inductively coupled plasma. The main goals of the study were (1) to determine how the operating conditions ( $\text{HBr}/\text{Cl}_2$  mixing ratio, input power, and bias power) influence the Si and  $\text{SiO}_2$  etching kinetics through the changes in gas-phase plasma characteristics (electron temperature, energy of ion bombardment, densities, and fluxes of plasma active species); and (2) to establish the gas-phase-related parameters that determine Si and  $\text{SiO}_2$  etching mechanisms under a given set of process conditions.

## Experimental and Modeling Details

### Experimental Setup, Procedures, and Conditions

The experiments were performed in the inductively coupled plasma (ICP) reactor, described in our previous works [19, 25]. Plasma was excited using a 13.56 MHz RF power supply connected to a flat copper coil on the top side of the reactor chamber. The coil had a cylindrical shape ( $r = 16$  cm,  $l = 12.8$  cm) and was made from anodized aluminum. Another 12.56 MHz RF power supply was used to produce the negative dc bias voltage ( $-U_{dc}$ ) on the bottom electrode. The experiments were conducted at constant gas pressure ( $p = 10$  mTorr) and total gas flow rate ( $q = 45$  sccm) while the variable parameters were input power ( $W = 500\text{--}800$  W), bias power ( $W_{dc} = 200\text{--}400$  W), and the  $\text{Cl}_2$  fraction in a feed gas. The initial content of each component in the  $\text{HBr} + \text{Cl}_2 + \text{O}_2$  gas mixture was adjusted through the corresponding partial flow rates  $q_{\text{HBr}}$ ,  $q_{\text{Cl}_2}$  and  $q_{\text{O}_2}$ . Accordingly, the composition of the feed gas was characterized by mole fractions  $y_i = q_i/q$ , where  $y_{\text{HBr}} + y_{\text{Cl}_2} + y_{\text{O}_2} = 1$ , or 100%.

During the etching experiments, samples of Si and  $\text{SiO}_2$  with dimensions of roughly  $2 \times 2$  cm<sup>2</sup> were located in the middle part of the bottom electrode. The bottom electrode was equipped with a built-in water-flow cooling system in order to maintain the constant sample temperatures at  $\sim 17$  °C. The Si and  $\text{SiO}_2$  etching rates were calculated as  $R = \Delta h/\tau$ , where  $\Delta h$  is the etched depth measured by the surface profiler Alpha-Step 500 (Tencor), and  $\tau = 2$  min is the processing time. In order to supply the measurements of  $\Delta h$ , we developed a line masking of the etched samples by the photoresist AZ1512. The thickness of the photoresist layer was  $\sim 1.5$   $\mu\text{m}$ .

The internal plasma parameters were examined using the double Langmuir probe tool DLP2000 (Plasmat Inc.). The data on electron temperature ( $T_e$ ) and ion current density ( $J_+$ ) were extracted from the I–V curves using the well-known statements of the double Langmuir probe theory [26, 27]. The total density of positive ions was calculated as  $n_+ \approx J_+/0.61ev_B$  [27], where  $v_B \approx \sqrt{eT_e/m_i}$  is the ion Bohm velocity without accounting

for negative ions. The ion-type-averaged ion mass was determined as  $m_i = \left( \sum y_{X_i^+} / m_{X_i^+} \right)^{-1}$ ,

where  $y_{X_i^+}$  and  $m_{X_i^+}$  are partial ion fractions and masses, respectively. Partial fractions of positive ions were roughly estimated under following assumptions: (1) Each type of neutral particle produces one type of parent positive ion; (2) Heterogeneous loss of positive ions dominates over both ion-ion and ion–electron recombinations in bulk plasma; (3) Probabilities of heterogeneous recombination are equal to 1 for all types of positive ions. Accordingly, corresponding loss frequencies (first-order rate coefficients) are  $2\nu_B(h_R l + h_L r) / r l$ , where  $h_R, h_L = f(\lambda_{X^+})$  are correction factors for radial and axial sheath sizes, and  $\lambda_{X^+}$  is the ion mean free path; (4) All types of positive ions may be characterized by close  $\lambda_{X^+}$  values. All these allow one to assume that, for the given type of positive ion,  $y_{X^+} \sim k_{iz} y_X / \sqrt{1/m_{X^+}}$ , where  $k_{iz}$  is the ionization rate coefficient [19, 20], and  $y_X$  is the fraction of corresponding neutral particle. Unfortunately, the more accurate estimation of  $m_i$  (with accounting for differences in ion mean free paths, see Ref. [31]) for the given gas mixture was impossible owing to a lack of ion-neutral scattering data. However, this issue does not bring a principal distortion in both treatment of Langmuir probe data and further analysis due to the rather low sensitivity of heterogeneous loss frequency to  $\lambda_{X^+}$ . Particularly, the change of  $\lambda_{X^+}$  by 2 times (or by 100%) causes  $\sim 30\%$  uncertainty in  $y_{X^+}$ . Even if the same error is transferred to  $m_i$ , the uncertainty in  $n_+$  appears to be less than 10%. The last value did not exceed the uncertainties in other parameters involved in both Langmuir probe data analysis and plasma modeling. It should be noted also that, under the given set of process conditions, the dominant contribution to  $m_i$  comes from  $\text{HBr}^+$  (for  $y_{\text{Cl}_2} < 20\%$ ) and  $\text{Cl}_2^+$  (for  $y_{\text{Cl}_2} > 30\%$ ) which have close masses. That is why, under the given set of process conditions, both absolute value and relative change of  $m_i$  are mainly determined by the differences in  $k_{iz} y_X$  parameters for  $\text{HBr}$  and  $\text{Cl}_2$  molecules. The applicability of the above simplification for  $\text{HBr}$ -,  $\text{Cl}_2$ - and  $\text{O}_2$ -based low pressure ( $p < 50$  mTorr) plasmas has been demonstrated in our previous studies [28–30].

## Plasma Modeling

In order to analyze the chemistry of plasma active species, we developed a simplified 0-dimensional (global) kinetic model [20, 28–30] using the experimental data of  $T_e$  and  $n_+$  as input parameters. The set of chemical reactions included in the model (Table 1) was composed on the basis of previous works that dealt with the modeling of  $\text{HBr} + \text{Ar}$  [20, 28],  $\text{Cl}_2 + \text{Ar}$  [29, 32, 33],  $\text{O}_2 + \text{Ar}$  [30, 32, 33],  $\text{Cl}_2 + \text{O}_2$  [32, 34], and  $\text{HBr} + \text{Cl}_2$  [19] plasmas. As given kinetic schemes (reaction sets with corresponding rate coefficients) for  $\text{HBr}$ ,  $\text{Cl}_2$  and  $\text{O}_2$  demonstrated an acceptable agreement between model-predicted and measured plasma parameters [29, 31–33], related issues were not the subject of discussion in this study. We also neglected the influence of dissociative attachment, charge transfer and ion-ion recombination processes on the neutral species kinetics. Under the given set of process conditions, contributions of these processes to total formation and decay rates for both atomic and molecular species are much lower (by  $\sim 2$  order of magnitude or even more) compared with those of electron-impact dissociations and heterogeneous recombinations. The model used the following assumption and simplifications:

- For the investigated range of process conditions, electron energy distribution functions (EEDFs) are close to Maxwellian ones [35]. The postulation of Maxwellian EEDF allows one to obtain rate coefficients for electron-impact processes R1–R17 as

**Table 1** The reduced reaction set describing the chemistry of neutral species in HBr + Cl<sub>2</sub> + O<sub>2</sub> plasma

Process	$k$ (cm <sup>3</sup> /s)	Process	$k$ (cm <sup>3</sup> /s)
1. HBr + e → H + Br + e	$f(T_e)$	58. BrO + BrO → O <sub>2</sub> + Br <sub>2</sub>	$1.5 \times 10^{-13}$
2. Br <sub>2</sub> + e → 2Br + e	$f(T_e)$	59. ClO + H → OH + Cl	$1.0 \times 10^{-16}$
3. H <sub>2</sub> + e → 2H + e	$f(T_e)$	60. ClO + Cl → Cl <sub>2</sub> + O	$1.0 \times 10^{-16}$
4. Cl <sub>2</sub> + e → 2Cl + e	$f(T_e)$	61. ClO + O → O <sub>2</sub> + Cl	$7.0 \times 10^{-11}$
5. O <sub>2</sub> + e → 2O + e	$f(T_e)$	62. ClO + O( <sup>1</sup> D) → O <sub>2</sub> + Cl	$1.0 \times 10^{-10}$
6. O <sub>2</sub> + e → 2O + e	$f(T_e)$	63. 2ClO → Cl <sub>2</sub> + O <sub>2</sub>	$1.5 \times 10^{-13}$
7. O <sub>2</sub> + e → O + O( <sup>1</sup> D) + e	$f(T_e)$	64. ClO + OH → HCl + O <sub>2</sub>	$5.0 \times 10^{-13}$
8. O + e → O( <sup>1</sup> D) + e	$f(T_e)$	65. HOBr + H → H <sub>2</sub> + BrO	$1.5 \times 10^{-15}$
9. HCl + e → H + Cl + e	$f(T_e)$	66. HOBr + Br → OH + Br <sub>2</sub>	$2.5 \times 10^{-17}$
10. BrCl + e → Br + Cl + e	$f(T_e)$	67. HOBr + O → OH + BrO	$1.5 \times 10^{-11}$
12. BrO + e → Br + O + e	$f(T_e)$	68. HOBr + O( <sup>1</sup> D) → OH + BrO	$1.0 \times 10^{-10}$
13. ClO + e → Cl + O + e	$f(T_e)$	69. HOBr + OH → H <sub>2</sub> O + BrO	$5.0 \times 10^{-13}$
14. HOBr + e → OH + Br + e	$f(T_e)$	70. HOCl + Cl → HCl + ClO	$1.2 \times 10^{-14}$
15. HOCl + e → OH + Cl + e	$f(T_e)$	71. HOCl + Cl → OH + Cl <sub>2</sub>	$2.0 \times 10^{-12}$
16. H <sub>2</sub> O + e → H + OH + e	$f(T_e)$	72. HOCl + H → OH + HCl	$6.0 \times 10^{-12}$
17. OH + e → O + H + e	$f(T_e)$	73. HOCl + H → H <sub>2</sub> + ClO	$8.0 \times 10^{-15}$
18. HBr + H → H <sub>2</sub> + Br	$1.2 \times 10^{-11}$	74. HOCl + O → OH + ClO	$3.0 \times 10^{-13}$
19. HBr + Br → Br <sub>2</sub> + H	$1.4 \times 10^{-29}$	75. HOCl + OH → H <sub>2</sub> O + ClO	$5.0 \times 10^{-13}$
20. HBr + O → OH + Br	$3.6 \times 10^{-13}$	76. H <sub>2</sub> O + O → OH + OH	$1.0 \times 10^{-18}$
21. HBr + O( <sup>1</sup> D) → OH + Br	$1.5 \times 10^{-10}$	77. H <sub>2</sub> O + O( <sup>1</sup> D) → OH + OH	$2.0 \times 10^{-10}$
22. HBr + OH → H <sub>2</sub> O + Br	$8.0 \times 10^{-12}$	78. H <sub>2</sub> O + Cl → OH + HCl	$3.0 \times 10^{-18}$
23. HBr + BrO → HOBr + Br	$2.0 \times 10^{-14}$	79. H <sub>2</sub> O + Br → OH + HBr	$1.0 \times 10^{-20}$
24. HBr + ClO → HOCl + Br	$5.0 \times 10^{-15}$	80. OH + H → H <sub>2</sub> + O	$6.0 \times 10^{-15}$
25. HBr + Cl → HCl + Br	$1.9 \times 10^{-11}$	81. OH + O → O <sub>2</sub> + H	$3.0 \times 10^{-11}$
26. Br <sub>2</sub> + H → HBr + Br	$1.2 \times 10^{-10}$	82. OH + O( <sup>1</sup> D) → O <sub>2</sub> + H	$1.0 \times 10^{-10}$
27. Br <sub>2</sub> + O → BrO + Br	$1.3 \times 10^{-11}$	83. OH + Br → HBr + O	$1.0 \times 10^{-20}$
28. Br <sub>2</sub> + O( <sup>1</sup> D) → BrO + Br	$1.3 \times 10^{-10}$	84. OH + Cl → HCl + O	$3.0 \times 10^{-14}$
29. Br <sub>2</sub> + OH → HOBr + Br	$3.1 \times 10^{-11}$	85. OH + OH → H <sub>2</sub> O + O	$2.0 \times 10^{-12}$
30. Br <sub>2</sub> + Cl → Br + BrCl	$1.5 \times 10^{-10}$	86. BrCl + Br → Br <sub>2</sub> + Cl	$3.5 \times 10^{-15}$
31. H <sub>2</sub> + Br → HBr + H	$1.6 \times 10^{-18}$	87. BrCl + Cl → Cl <sub>2</sub> + Br	$1.5 \times 10^{-11}$
32. H <sub>2</sub> + O → OH + H	$2.0 \times 10^{-15}$	88. BrCl + O → BrO + Cl	$2.0 \times 10^{-11}$
33. H <sub>2</sub> + O( <sup>1</sup> D) → OH + H	$9.0 \times 10^{-11}$	89. BrCl + O( <sup>1</sup> D) → BrO + Cl	$1.0 \times 10^{-10}$
34. H <sub>2</sub> + OH → H <sub>2</sub> O + H	$1.3 \times 10^{-13}$	90. BrCl + OH → HOBr + Cl	$1.5 \times 10^{-12}$
35. H <sub>2</sub> + BrO → HBr + OH	$1.0 \times 10^{-20}$	91. Cl → Cl <sub>ads</sub>	$f(\gamma), \gamma = 0.05$
36. H <sub>2</sub> + Cl → HCl + H	$2.5 \times 10^{-13}$	Cl <sub>ads</sub> + H → HCl	
37. H <sub>2</sub> + ClO → HCl + OH	$1.0 \times 10^{-20}$	Cl <sub>ads</sub> + O → ClO	
37. Cl <sub>2</sub> + H → HCl + Cl	$4.0 \times 10^{-11}$	Cl <sub>ads</sub> + Cl → Cl <sub>2</sub>	
39. Cl <sub>2</sub> + Br → BrCl + Cl	$2.0 \times 10^{-15}$	Cl <sub>ads</sub> + Br → BrCl	
40. Cl <sub>2</sub> + O → ClO + Cl	$3.0 \times 10^{-13}$	Cl <sub>ads</sub> + OH → HOCl	

**Table 1** (continued)

Process	$k$ (cm <sup>3</sup> /s)	Process	$k$ (cm <sup>3</sup> /s)
41. Cl <sub>2</sub> + O( <sup>1</sup> D) → ClO + Cl	3.6 × 10 <sup>-11</sup>	92. Br → Br <sub>ads</sub>	$f(\gamma)$ , $\gamma = 0.1$
42. Cl <sub>2</sub> + OH → HOCl + Cl	3.6 × 10 <sup>-13</sup>	Br <sub>ads</sub> + H → HBr	
43. HCl + Cl → Cl <sub>2</sub> + H	3.0 × 10 <sup>-28</sup>	Br <sub>ads</sub> + O → BrO	
44. HCl + Br → HBr + Cl	1.0 × 10 <sup>-15</sup>	Br <sub>ads</sub> + Cl → BrCl	
45. HCl + H → H <sub>2</sub> + Cl	4.4 × 10 <sup>-13</sup>	Br <sub>ads</sub> + Br → Br <sub>2</sub>	
46. HCl + O → OH + Cl	9.0 × 10 <sup>-15</sup>	Br <sub>ads</sub> + OH → HOBr	
47. HCl + O( <sup>1</sup> D) → OH + Cl	1.0 × 10 <sup>-10</sup>	93. O → O <sub>ads</sub>	$f(\gamma)$ , $\gamma = 0.1$
48. HCl + OH → H <sub>2</sub> O + Cl	1.5 × 10 <sup>-12</sup>	O <sub>ads</sub> + H → OH	
49. HCl + ClO → HOCl + Cl	1.0 × 10 <sup>-15</sup>	O <sub>ads</sub> + O → O <sub>2</sub>	
50. HCl + BrO → HOBr + Cl	1.0 × 10 <sup>-15</sup>	O <sub>ads</sub> + Cl → ClO	
51. BrO + H → OH + Br	1.0 × 10 <sup>-16</sup>	O <sub>ads</sub> + Br → BrO	
52. BrO + Br → Br <sub>2</sub> + O	1.0 × 10 <sup>-16</sup>	94. H → H <sub>ads</sub>	$f(\gamma)$ , $\gamma = 0.01$
53. BrO + O → O <sub>2</sub> + Br	3.0 × 10 <sup>-11</sup>	H <sub>ads</sub> + H → H <sub>2</sub>	
54. BrO + O( <sup>1</sup> D) → O <sub>2</sub> + Br	1.0 × 10 <sup>-10</sup>	H <sub>ads</sub> + O → OH	
55. BrO + OH → O <sub>2</sub> + HBr	1.0 × 10 <sup>-12</sup>	H <sub>ads</sub> + Cl → HCl	
56. BrO + ClO → O <sub>2</sub> + BrCl	6.0 × 10 <sup>-13</sup>	H <sub>ads</sub> + Br → HBr	
57. BrO + BrO → O <sub>2</sub> + 2Br	3.0 × 10 <sup>-12</sup>	H <sub>ads</sub> + OH → H <sub>2</sub> O,	

functions of  $T_e$  in the form of  $k = AT_e^B \exp(-C/T_e)$ . Parameters  $A$ ,  $B$  and  $C$  for feed gas components as well as for their by-products were either found in Refs. [19, 20, 30, 32] or estimated with the known dissociation cross-sections [36, 37].

- The gas temperature was assumed to be a linear function of the input power ( $T_{gas} = 600\text{--}750$  K for  $W = 500\text{--}800$  W) and independent of both feed gas composition and bias power. The statement that  $T_{gas} \approx 700$  K at  $p = 10$  mTorr and  $W = 700$  W is in agreement with our previous experimental and modeling works in the given ICP reactor [28–30]. The rate coefficients for R18–R90 for actual values of  $T_{gas}$  were taken from the NIST Chemical Kinetics Database [38].
- The heterogeneous decay of atomic species follows the Eley–Rideal kinetics. Accordingly, the rate coefficients (decay frequencies) for R91–R94 may be evaluated as  $k_S \approx \gamma v_T / \Lambda$ , where  $\Lambda = [(2.405/r)^2 + (\pi/l)^2]^{-1/2}$  is the diffusion length [33, 35],  $v_T = (8k_B T_{gas} / \pi m)^{1/2}$ , and  $\gamma$  is the recombination probability. Recombination probabilities for Br ( $\gamma_{Br} \approx 0.1$ ), Cl ( $\gamma_{Cl} \approx 0.05$ ), O ( $\gamma_O \approx 0.1$ ), and H ( $\gamma_H \approx 0.01$ ) species were taken from experimental works [39–43]. Furthermore, we assumed equal probabilities for all parallel reaction pathways between adsorbed (marked by the “ads” subscript) and gaseous species.
- The total ion flux to the etched sample (from bulk plasma toward the bottom electrode) is  $\Gamma_+ \approx h_L v_{Bn_+}$  [33, 35, 44]. The calculation of  $h_L$  requires the ion-type-averaged mean free path which, in fact, is not available owing to a lack of ion-neutral scattering data. At the same time, our previous works [28, 29] indicated a fairly good quantitative agreement between the model-predicted  $e\Gamma_+$  and measured  $J_+$  in Cl<sub>2</sub> + Ar and HBr + Ar plasmas under the close range of experimental conditions. Accordingly, an assumption  $\Gamma_+ \approx J_+ / e$  was applied in this work.

The electron density ( $n_e$ ) was extracted from the measured  $n_+$  using the solution of the steady-state chemical kinetic equation for negative ions together with the quasi-neutrality equation [19, 20]. This allows one to obtain

$$n_e \approx \frac{k_{ii}n_+^2}{v_{da} + k_{ii}n_+}$$

where  $k_{ii} \approx 10^{-7}$  cm<sup>3</sup>/s is the averaged rate coefficient for ion-ion recombination [20], and  $v_{da} = \sum k_{da}n$  is the total frequency of dissociative attachment. Dissociative attachment rate coefficients  $k_{da}$  (in fact, parameters  $A$ ,  $B$  and  $C$  for above fitting expression) for dominant electronegative components with the volume density were either directly taken from Refs. [19, 20, 30, 32] or estimated using known process cross-sections [36, 37] and data for other species. The adequacy of the given modeling algorithm was confirmed in our previous works [19, 28–30].

## Results and Discussion

### Etching Rates and Selectivities

Figure 1 illustrates the influence of input process parameters on both Si and SiO<sub>2</sub> etching rate as well as on the Si/SiO<sub>2</sub> etching selectivity. As shown in Fig. 1a, an increase in  $y_{Cl_2}$  results in monotonically increasing rates for Si, SiO<sub>2</sub>, and the photoresist. The similar effect of  $y_{Cl_2}$  on the etching rates of poly-Si, SiO<sub>2</sub> and Si<sub>3</sub>N<sub>4</sub> has been reported by Yeom et al. [12] for HBr+Cl<sub>2</sub> plasma. The faster change in  $R_{Si}$  (11–61 nm/min, or by ~6 times for 0–89% Cl<sub>2</sub>) compared with  $R_{SiO_2}$  (7–20 nm/min, or by ~3 times for 0–89% Cl<sub>2</sub>) provides an increase in the Si/SiO<sub>2</sub> etching selectivity in the range of 1.7–3.4. Experiments also showed that, for any constant HBr/Cl<sub>2</sub> mixing ratio, effects of input power and bias power on both Si and SiO<sub>2</sub> etching rates are different. Particularly, an increase in  $W$  from 500 to 800 W for the 24% HBr+71% Cl<sub>2</sub>+5% O<sub>2</sub> gas mixture lowers etching rates for Si and SiO<sub>2</sub> from 75 to 36 nm/min and 17–11 nm/min, respectively (Fig. 1b). Accordingly, as the latter falls at a slightly slower rate, the  $R_{Si}/R_{SiO_2}$  ratio decreases from 4.3 to 3.2. In contrast, an increase in  $W_{dc}$  (and thus, in ion bombardment energy) was found to increase both etching rates (76–126 nm/min, or by ~1.7 times for Si and 18–23 nm/min, or by ~1.3 times for SiO<sub>2</sub> at  $W_{dc} = 200$ –400 W) and Si/SiO<sub>2</sub> etching selectivity in the range of 4.3–5.4 (Fig. 1c). It should be noted also that the etching rate of photoresist shows a similar increasing trend with both  $W$  (128–205 nm/min for 500–800 W) and  $W_{dc}$  (128–243 nm/min for 200–400 W). As such, the behavior of the photoresist etching rate versus input power contradicts those for Si and SiO<sub>2</sub>.

The decreases in both Si and SiO<sub>2</sub> etching rates with higher input powers, revealed by Fig. 1b, are unexpected. From earlier published works [1, 3, 5], it can be clearly seen that an increase in input power in HBr- and Cl<sub>2</sub>-based plasmas results in the same change in the etching rates for many materials. This effect is reasonably associated with increasing densities and fluxes of positive ions and halogen atoms due to increasing electron impact ionization and dissociation rates. In particular, McNevin et al. [17] observed increasing Si and SiO<sub>2</sub> etching rates with an increase in input power in pure Cl<sub>2</sub> plasma and in the Cl<sub>2</sub>+O<sub>2</sub> gas mixture with fixed fractions of components. Furthermore, Ref. [45] reported a similar increasing tendency for the Si etching rate for both HBr+Ar and Cl<sub>2</sub>+Ar plasmas.

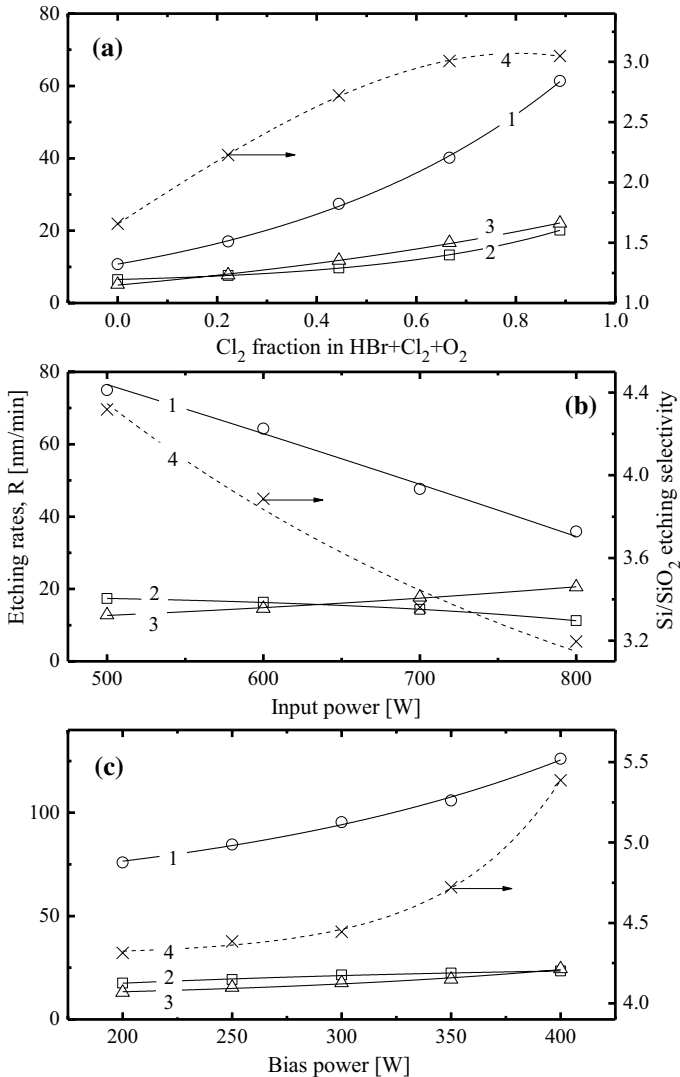


**Fig. 1** Etching rates for Si (1), SiO<sub>2</sub> (2), and photoresist (3), and the Si/SiO<sub>2</sub> etching selectivity (4) as functions of Cl<sub>2</sub> fraction in a feed gas (a), input power (b), and bias power (c) at =10 mTorr. The photoresist etching rate is reduced by 10 times in order to fit the scale. The process condition are: **a**  $y_{O_2} = 11\%$ ,  $W = 500$  W and  $W_{dc} = 200$  W; **b**  $y_{Cl_2} = 71\%$ ,  $y_{O_2} = 5\%$  and  $W_{dc} = 200$  W; **c**  $y_{Cl_2} = 71\%$ ,  $y_{O_2} = 5\%$  and  $W = 500$  W

It is known that the effect of input process parameters on the etching rate (in fact, on the rate of ion-assisted chemical reaction on the plasma-surface interface) depends on the etching regime that provides dominant chemical or physical etching pathways [5, 7, 35]. The factors determining the etching regime for a given combination of gas system and etched material are: (1) the fluxes of active species (chemically active neutrals, energetic ions) on the etched surface; (2) the ion bombardment energy; and (3) the volatility of reaction products. All these factors do influence the effective reaction probability between the etchant



species and surface atoms. By considering the similar chemical natures of both Si and SiO<sub>2</sub> etching products, and their nearly constant surface temperatures, one can surely assume that the relationships between input process parameters and etching rates are mainly controlled by factors (1) and (2). Therefore, in order to explain the experimentally obtained effects for the Si and SiO<sub>2</sub> etching rates, data on plasma parameters and densities of active species are needed.

## Gas-Phase Plasma Parameters and Densities of Active Species

The general regularities and mechanisms that determine the gas-phase plasma characteristics (internal plasma parameters, steady-state densities of plasma active species) in the binary HBr+Cl<sub>2</sub> gas mixture were the subjects of detailed discussion in our previous work [19]. As the current work deals with the ternary HBr+Cl<sub>2</sub>+O<sub>2</sub> system with  $y_{O_2} = \text{const}$ , and the process conditions are very close to those used in Ref. [19], we will just briefly summarize the most important results while accounting for an actual set of input parameters and the presence of oxygen in a feed gas.

Figures 2 and 3 illustrate the influence of variable process parameters on electron temperature and densities of charges species. The obtained effects may be described as follows:

- An increase in  $y_{Cl_2}$  from 0 to 89% (in fact, the full substitution of HBr for Cl<sub>2</sub> in the HBr+Cl<sub>2</sub>+11% O<sub>2</sub> gas mixture) causes a weak increase in  $T_e$  (2.5–2.8 eV, see Fig. 2a) due to the decreasing electron energy loss in inelastic collisions with gas species. This is because the higher dissociation degree for Cl<sub>2</sub> molecules compared with HBr provides a higher fraction of atomic species in the Cl<sub>2</sub>-rich plasmas. Accordingly, as the Cl atoms are characterized by higher threshold energies and lower cross-sections for electronic excitation and ionization compared with those for HBr, HCl, and Br, the substitution of HBr for Cl<sub>2</sub> enriches EEDF by the high-energy electrons and shifts  $T_e$  toward higher values. A similar effect has been reported for HBr+Ar and Cl<sub>2</sub>+Ar plasmas [28–30]. A growth in both  $n_+ = 2.5 \times 10^{10}$ – $3.5 \times 10^{10}$  cm<sup>-3</sup> and  $n_e = 2.1 \times 10^9$ – $7.8 \times 10^9$  cm<sup>-3</sup> (Fig. 3a) is the result of increasing total ionization frequency  $\nu_{iz} = \sum k_{iz}n$ , where  $k_{iz}$  and  $n$  are the ionization rate coefficient and the density for each type of neutral particle, respectively. This is due to the much higher  $k_{iz}$  for Cl<sub>2</sub> molecules ( $\sim 1.3 \times 10^{-9}$  cm<sup>3</sup>/s vs.  $\sim 6.7 \times 10^{-10}$  cm<sup>3</sup>/s for HBr and  $\sim 6.8 \times 10^{-10}$  cm<sup>3</sup>/s for Br at  $T_e = 3$  eV) and an increase in all  $k_{iz}$  together with increasing  $T_e$  (due to  $\epsilon_{iz} > 3/2 T_e$ , where  $\epsilon_{iz}$  is the threshold energy for ionization). Obviously, the behavior of the ion current density ( $J_+ = 0.5$ – $0.8$  mA/cm<sup>2</sup> for 0–89% Cl<sub>2</sub>, see Fig. 2a) directly correlates with  $n_+$ . Finally, a decrease in the  $n_-/n_e$  ratio (10.7–3.5 for 0–89% Cl<sub>2</sub>, see Fig. 3a) is the result of a nearly constant total negative ion density  $n_- \approx 2.7 \times 10^{10}$  cm<sup>-3</sup>. The last effect is due to the nearly proportional increase in both total attachment rate and ion-ion recombination frequency.
- An increase in input power directly influences  $n_e$  [35] ( $5.8 \times 10^9$ – $2.2 \times 10^{10}$  cm<sup>-3</sup> for 500–800 W, see Fig. 3b) and thus, increases the ionization rates for neutral species. As a result, one can obtain  $n_+ = 3.4 \times 10^{10}$ – $6.4 \times 10^{10}$  cm<sup>-3</sup> (Fig. 3b) and  $J_+ = 0.7$ – $1.4$  mA/cm<sup>2</sup> (Fig. 2b). The total attachment rate also increases providing  $n_- = 2.8 \times 10^{10}$ – $4.3 \times 10^{10}$  cm<sup>-3</sup> for  $W = 500$ – $800$  W. However, this tendency is much weaker than that for  $n_e$  because of decreasing densities of electronegative molecules, their's  $k_{da}$  (due to  $\epsilon_{da} \ll 3/2$ , where  $\epsilon_{da}$  is the threshold energy for dissociative attachment) as well as increasing ion-ion recombination frequency  $k_{ii}n_+$ . For these reasons, the parameter  $n_-/n_e$  characterizing plasma electronegativity decreases by more

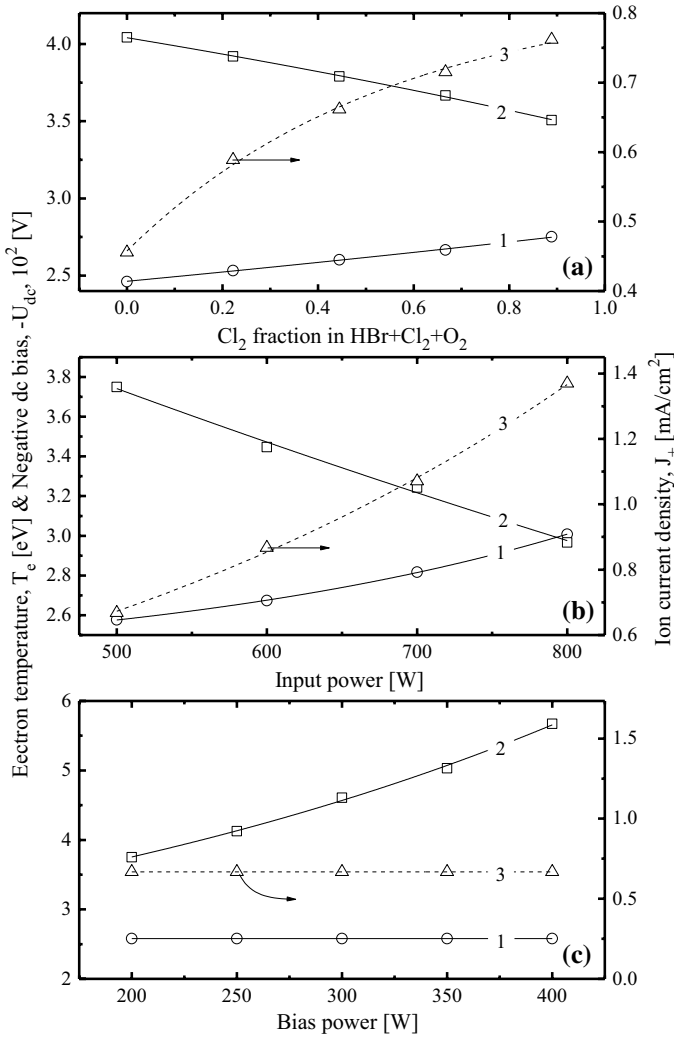


**Fig. 2** Electron temperature (1), negative dc bias (2), and ion current density (3) as functions of Cl<sub>2</sub> fraction in a feed gas (a), input power (b), and bias power (c). The process conditions correspond to Fig. 1

than two times (4.9–2.0 for  $W = 500$ –800 W, see (Fig. 3a)). A weak increase in  $T_e$  (2.6–3.0 eV for 500–800 W, see Fig. 2b) is also connected with decreasing fractions of molecular species that are characterized by the higher electron energy losses compared with atoms (mainly through the vibrational and low-threshold electronic excitations [35]).

- An increase in bias power does not influence  $T_e$  ( $\sim 2.6$  eV for  $W_{dc} = 200$ –400 W, see Fig. 2c) and  $n_e$  ( $\sim 5.8 \times 10^9$  cm<sup>-3</sup> for  $W_{dc} = 200$ –400 W, see Fig. 3c), which assumes that no changes in the electron-impact kinetics occur. Therefore, within the given model of plasma chemistry, the effect of  $W_{dc}$  on the densities of plasma active species may be neglected. Obviously, this finding reflects the main goal of the ICP etch-

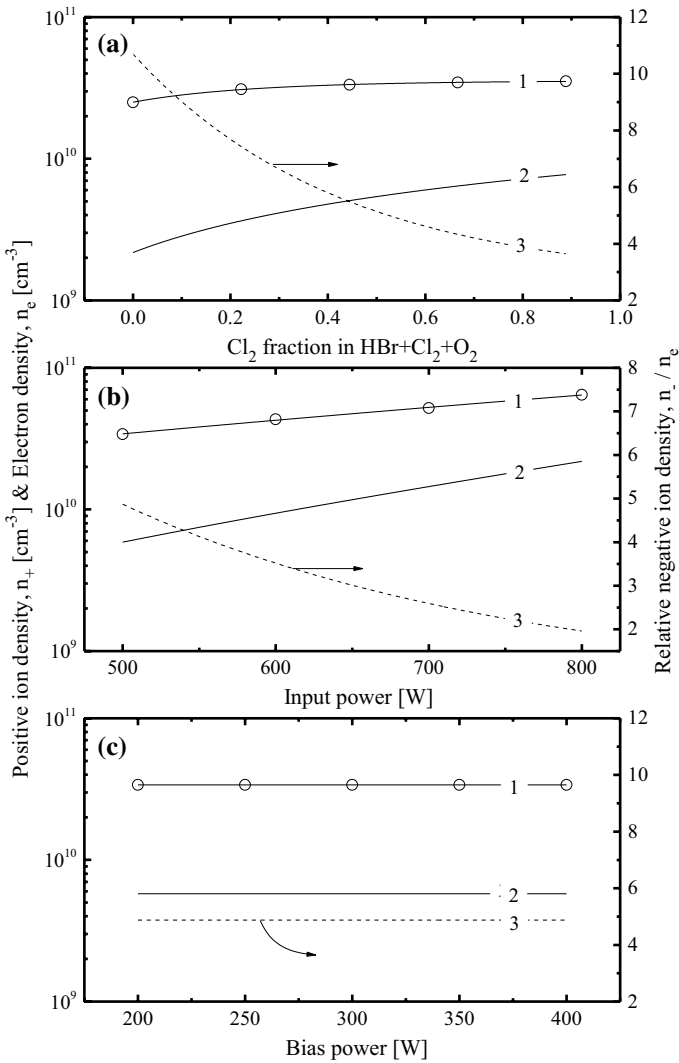


**Fig. 3** Positive ion density (1), electron density (2), and relative density of negative ions (3) as functions of  $\text{Cl}_2$  fraction in a feed gas (a), input power (b), and bias power (c). The process conditions correspond to Fig. 1

ing system, which is to provide an independent control of ion flux and ion bombardment energy [35].

Figure 4 shows the effects of  $y_{\text{Cl}_2}$  and input power on the steady-state densities of neutral species. It was found that, under the given set of process conditions, pure HBr plasma exhibits all earlier described features of neutral species kinetics [19, 20, 28]. These are as follows: (1) reactions R1 and R2 represent the nearly equal sources for the electron-impact formation of Br atoms; (2) the condition  $k_2 \gg k_3$  as well as the fast decay of H atoms through R18 and R26 results in  $n_{\text{Br}}/n_{\text{H}} \gg 1$ ; (3) high formation rates for  $\text{H}_2$  and  $\text{Br}_2$  in R18

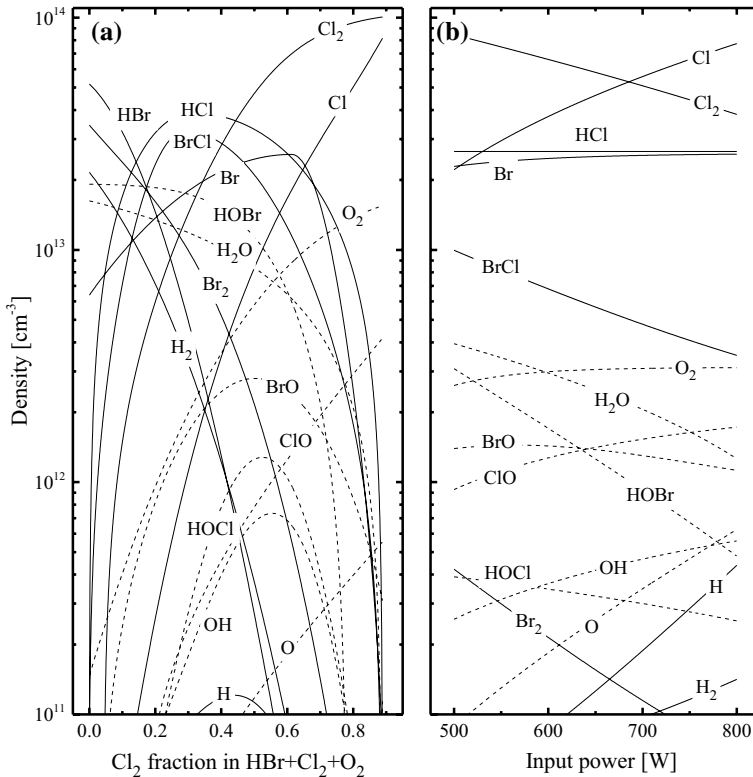


**Fig. 4** Steady-state densities of neutral species as functions of Cl<sub>2</sub> fraction in a feed gas (a) and input power (b). The process conditions correspond to Fig. 1

and R92 lead to  $n_{H_2}, n_{Br_2} \approx n_{Br}$ ; and (4) the effective recovery of the original HBr molecules through R26 allows for domination of this species over other neutral components. The transition to the 89% HBr + 11% O<sub>2</sub> gas mixture lowers the overall Br atom formation rate in R1 and R2, but supplies several additional channels for the dissociation of HBr (R20–R22) and Br<sub>2</sub> (R27–R29) owing to their interactions with O, O(<sup>1</sup>D), and OH. However, the conditions  $k_1 n_e \gg k_{20} n_O + k_{22} n_{OH}$  and  $k_2 n_e \gg k_{27} n_O + k_{29} n_{OH}$  imply that the efficiency of these channels is much lower compared with those of R1 and R2. Furthermore, one should remember that each reaction mechanism from the R27–R29 group liberates only one Br atom while the other one appears to be located in the BrO or HOBr molecule. All these suppress the total Br atom formation rate and result in a weak decrease in  $n_{Br}$  compared with pure HBr plasma.

The substitution of HBr for Cl<sub>2</sub> in the HBr + Cl<sub>2</sub> + 11% O<sub>2</sub> gas mixture provides the decreasing rates of R1 and R2, but simultaneously adds the Br atoms formation pathways through R25 and R30. As the latter have quite high rate coefficients, the fast decay of Cl, HBr, and Br<sub>2</sub>, as well as the rapidly increasing formation rates and densities for both HCl and BrCl are observed (Fig. 4a). In such cases, the reactions R9, R10, and R87 also begin to be an essential source of Br atoms in the range of 20–81% Cl<sub>2</sub>. Another important feature is that the rate coefficient for R20–R22 and R27–R29 are noticeably higher than those for R40–R42 (see Table 1). That is why an increase in  $y_{Cl_2}$  sufficiently reduces the

consumption rates for O, O(<sup>1</sup>D), and OH, provides the rapidly increasing densities of these species (by ~2.7 times for O, ~5.2 times for O(<sup>1</sup>D) and ~3.7 times for OH at 0–21% Cl<sub>2</sub>, see Fig. 4a) and accelerates the dissociation of both HBr and Br<sub>2</sub> through R20–R22 and R27–R29. All these effects, together with increasing electron impact dissociation frequencies for both HBr ( $k_1 n_e = 2.0\text{--}9.7\text{ s}^{-1}$  for 0–89% Cl<sub>2</sub>) and Br<sub>2</sub> ( $k_2 n_e = 19\text{--}82\text{ s}^{-1}$  for 0–89% Cl<sub>2</sub>), results in non-monotonic behavior for both the effective Br atom formation rate and  $n_{Br}$ . The density of Cl atoms increase monotonically, but slower than expected from the linear change in  $y_{Cl_2}$ . This is due to the high Cl atom consumption rate through R25, R30, and R87 in the HBr-rich plasmas.

A growth in input power results in increasing electron-impact dissociation rates for all molecular species, but has different effects on the densities of Br and Cl atoms. In particular, the data of Fig. 4b and Table 1 show that the main source of Cl atoms under the condition  $y_{Cl_2} \gg y_{Br_2}$  is the electron-impact dissociation of Cl<sub>2</sub> through R4. Accordingly, the change in input power from 500 to 800 W increases the Cl<sub>2</sub> dissociation frequency ( $k_4 n_e = 50\text{--}234\text{ s}^{-1}$ , or by ~4.7 times) and results in a nearly proportional increase in both Cl<sub>2</sub> dissociation degree and  $n_{Cl}$  ( $2.2 \times 10^{13}\text{--}7.7 \times 10^{13}\text{ cm}^{-3}$ ). As for Br atoms, their dominant formation pathways are reactions R10 and R14 with the participation of BrCl and HOBr, respectively. Though these species also exhibit increasing dissociation degrees and decreasing densities toward higher input powers (by ~2.9 times for BrCl and ~6.5 times for HOBr at 500–800 W), one can obtain only very weak growth in  $n_{Br}$ , as the Br atoms are effectively bonded in the form of BrO through R92. The last process is supported by the rapidly increasing O atom density ( $8.5 \times 10^{10}\text{--}6.3 \times 10^{11}\text{ cm}^{-3}$ , or by ~7.4 times for 500–800 W) due to increasing O atom formation rates in R6 and R7 and decreasing O atom consumption rate through R27 due to decreasing  $n_{Br_2}$ .

Summarizing the above data, one can conclude that changes in  $y_{Cl_2}$  and input power have similar effects on the gas-phase plasma parameters that are the core interest of the etching process analysis. In particular, an increase in both input parameters at the constant other ones results in (1) monotonically increasing ion current densities ( $J_+ = 0.5\text{--}0.8\text{ mA/cm}^2$  for 0–89% Cl<sub>2</sub> and 0.7–1.4 mA/cm<sup>2</sup> for 500–800 W) that determine the ion flux on the etched surface; (2) monotonically increasing total density of etchant species ( $n_{Br} + n_{Cl} = 6.4 \times 10^{12}\text{--}8.0 \times 10^{13}\text{ cm}^{-3}$  for 0–89% Cl<sub>2</sub> and  $4.5 \times 10^{13}\text{--}1.0 \times 10^{14}\text{ cm}^{-3}$  for 500–800 W); and (3) a monotonically increasing density of O atoms. Against this background, the different behaviors of both Si and SiO<sub>2</sub> etching rates versus  $y_{Cl_2}$  and  $W$  look strange. Moreover, opposite behaviors for  $R = f(W)$  from Fig. 1b and the changes in  $J_+$ , as well as partial and total densities of etchant species from Figs. 2b and 4b, do not allow one to attribute the obtained effects neither to the ion-flux- nor to the neutral-flux-limited etching regime of ion-assisted chemical reactions. Thus, in order to answer the question on peculiarities of the Si and SiO<sub>2</sub> etching mechanisms in the HBr + Cl<sub>2</sub> + O<sub>2</sub> gas system, a more detailed analysis of etching kinetics is required.

## The Relationships Between Plasma Chemistry and Etching Kinetics

According to Refs. [46–48], in general, the rate of ion-assisted heterogeneous chemical reactions may be expressed as  $R = \gamma_R \Gamma$ , where  $\Gamma$  is the flux of chemically active neutral species, and  $\gamma_R \approx s_0(1 - \theta)$  is the reaction probability. For different reaction regimes,  $\gamma_R$  may be either constant at a constant surface temperature ( $\gamma_R \approx s_0$  for  $\theta \rightarrow 0$ , where  $s_0$  is the sticking coefficient for etchant species, and  $\theta$  is the fraction of active surface sites occupied by reaction products) or dependent on both neutral and ion fluxes through  $\theta$ . From several

published works, it can be understood that (1) the differences in the halogenation degrees for Si surfaces exposed to pure  $\text{Cl}_2$  and HBr plasmas are in agreement with the differences in corresponding atom size [9]; (2) the differences in silicon etching rates in pure  $\text{Cl}_2$  and HBr plasmas [12, 23, 24] are in agreement with the differences in corresponding halogen atom and ion fluxes [8, 19, 20]; (3) the Si etching yields pure  $\text{Cl}_2$  and HBr plasmas at one and the same ion bombardment energy are very close [8]; and (4) the change in Si etching yield with variations of  $\text{Cl}_2/\text{HBr}$  mixing ratio at constant ion bombardment energy does not exceed the experimental error [8]. It is important to note that both ionic and neutral fractions in Ref. [8] were quite similar to our case. In addition, Ito et al. [49] reported about very close Si etching yields by  $\text{Cl}^+$ ,  $\text{Br}^+$  and  $\text{HBr}^+$  ions in ion beam experiments. Furthermore, they found that the injection of  $\text{H}^+$  ions or H atoms with an amount of  $\sim 10$  times higher than that for  $\text{Br}^+$  had no influence on Si etching yield. Therefore, taking into account the very low density of H atoms under the conditions of current study, one can assume no effect of hydrogen on both Br and Cl atom reaction kinetics as well as suggest the effective reaction probabilities for Br and Cl atoms with Si surface being quite close. Unfortunately, we cannot provide the same analysis for  $\text{SiO}_2$  because the corresponding data are just absent. However, our experiment showed that Si and  $\text{SiO}_2$  etching rates always change in one and the same manner that probably points out on the same etching mechanisms for both materials. As such, the suggestion on close effective reaction probabilities for Cl and Br atoms with  $\text{SiO}_2$  may also be applied. All these allow one to operate with the total chemical active flux  $\Gamma_{\text{Br}} + \Gamma_{\text{Cl}}$  when analyzing the Si and  $\text{SiO}_2$  etching kinetics. Accordingly, the  $R/(\Gamma_{\text{Br}} + \Gamma_{\text{Cl}})$  ratios for Si and  $\text{SiO}_2$  directly reflect the influence of input process parameters on the effective (the atom-type-averaged, by other words) probabilities of chemical reactions between the halogen atoms and the etched material— $\gamma_{R,\text{Si}}$  and  $\gamma_{R,\text{SiO}_2}$ . The substitution of HBr for  $\text{Cl}_2$  in the  $\text{HBr} + \text{Cl}_2 + \text{O}_2$  feed gas (Fig. 5a) results in monotonically increasing  $\Gamma_{\text{Br}} + \Gamma_{\text{Cl}}$  ( $6.4 \times 10^{16}$ – $1.2 \times 10^{18}$   $\text{cm}^{-2} \text{ s}^{-1}$  for 0–89%  $\text{Cl}_2$ ) that appears to be faster than the corresponding changes in both Si and  $\text{SiO}_2$  etching rates. Obviously, such a situation results in a decrease in  $R/(\Gamma_{\text{Br}} + \Gamma_{\text{Cl}})$  ( $1.7 \times 10^{-15}$ – $5.2 \times 10^{-16}$  for Si and  $1.0 \times 10^{-15}$ – $1.7 \times 10^{-16}$  for  $\text{SiO}_2$  at 0–89%  $\text{Cl}_2$ ) and points out on decreasing  $\gamma_{R,\text{Si}}$  and  $\gamma_{R,\text{SiO}_2}$ . A similar situation takes place for the effect of input power (Fig. 5b), where the growth in  $\Gamma_{\text{Br}} + \Gamma_{\text{Cl}}$  from  $5.6 \times 10^{17}$ – $1.6 \times 10^{18}$   $\text{cm}^{-2} \text{ s}^{-1}$  for 500–800 W corresponds to a fall in  $\gamma_{R,\text{Si}} \sim R_{\text{Si}}/(\Gamma_{\text{Br}} + \Gamma_{\text{Cl}})$  by about six times and  $\gamma_{R,\text{SiO}_2} \sim R_{\text{SiO}_2}/(\Gamma_{\text{Br}} + \Gamma_{\text{Cl}})$  by about four times. However, an increase in bias power (Fig. 5c) results in an increasing  $R/(\Gamma_{\text{Br}} + \Gamma_{\text{Cl}})$  ratio ( $1.4 \times 10^{-15}$ – $2.3 \times 10^{-15}$  for Si and  $3.1 \times 10^{-16}$ – $4.3 \times 10^{-16}$  for  $\text{SiO}_2$  at 250–400 W) due to the corresponding increase in  $R$  at  $\Gamma_{\text{Br}} + \Gamma_{\text{Cl}} = \text{const}$ . Therefore, though the changes in  $y_{\text{Cl}_2}$  and  $W$  have different effects on the absolute Si and  $\text{SiO}_2$  etching rates, their influence on both  $\gamma_{R,\text{Si}}$  and  $\gamma_{R,\text{SiO}_2}$  is quite close. This finding confirms that both materials have similar etching mechanisms and shows that a general agreement exists between experimental and modeling data. However, the obtained changes in  $\gamma_{R,\text{Si}}$  and  $\gamma_{R,\text{SiO}_2}$  require additional explanations.

From Refs. [46, 47], it can be understood that the probability of an ion-assisted chemical reaction is controlled by several ion-surface interaction pathways. In our case, these are: (1) the ion-stimulated desorption of reaction products, as the boiling points for both  $\text{SiCl}_4$  ( $\sim 58$  °C) and  $\text{SiBr}_4$  ( $\sim 154$  °C) [50] exceed the process temperature; and (2) the destruction of Si–O bonds, as the corresponding bond strength ( $\sim 800$  kJ/mol) is much higher for than for Si–Br ( $\sim 358$  kJ/mol) Si–Cl ( $\sim 416$  kJ/mol) [50]. The partial rate of each ion-driven pathway is  $Y_S \Gamma_+$ , where  $Y_S$  is the ion-type-averaged process yield. As  $Y_S$  has a sputtering yield, it is determined by the momentum transferred from the incident ion in a single collision [35, 51]. Therefore, one can assume  $Y_S \sim \sqrt{m_i \varepsilon_i}$ , where  $m_i$  is the effective ion mass,

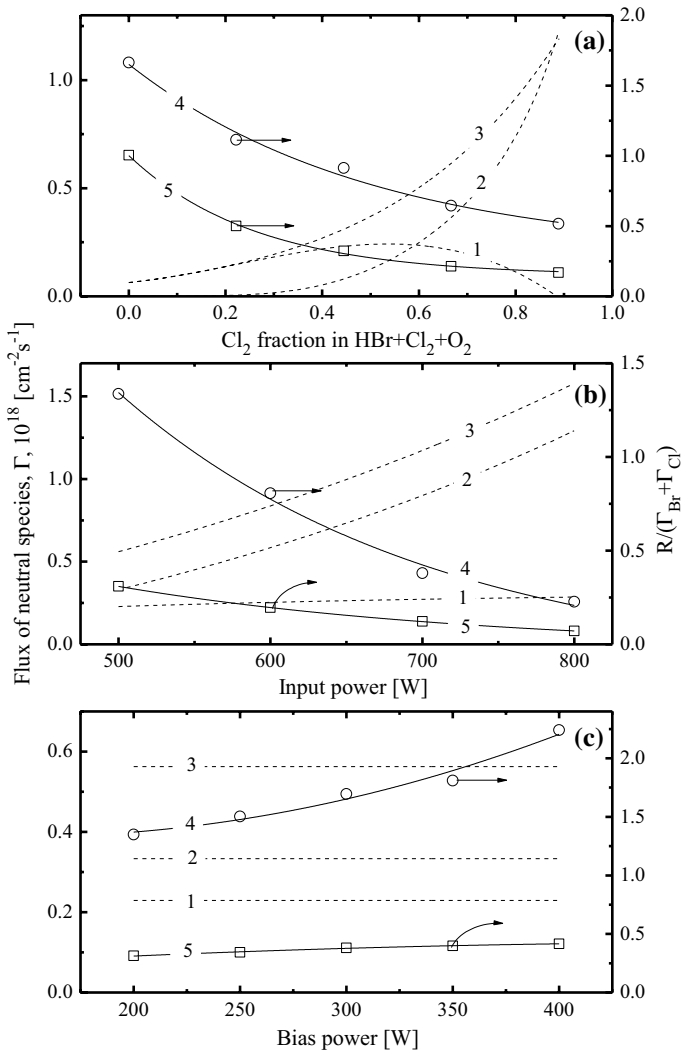


**Fig. 5** Fluxes of halogen atoms (1—Br, 2—Cl, 3—Br + Cl) and the parameter  $R/(\Gamma_{Br} + \Gamma_{Cl})$  characterizing the effective reaction probability for Si (4) and SiO<sub>2</sub> (5) as functions of Cl<sub>2</sub> fraction in a feed gas (a), input power (b), and bias power (c). The process conditions correspond to Fig. 1

$\epsilon_i \approx e| -U_f - U_{dc} |$  is the ion bombardment energy, and  $-U_f \approx 0.5T_e \ln(m_e/2.3m_i)$  is the floating potential. Accordingly, the influence of the input process parameters on the kinetics of both ion-stimulated desorption of reaction products and Si–O bond breaking may be characterized by the parameter  $\sqrt{m_i \epsilon_i} \Gamma_+$  or  $\sqrt{M_i \epsilon_i} \Gamma_+$ , where  $M_i$  is the effective ion molar mass. From Fig. 2a, one can see that an increase in  $y_{Cl_2}$  results in decreases in both  $-U_{dc}$  (404–351 V for 0–89% Cl<sub>2</sub>) and ion bombardment energy (420–368 eV for 0–89% Cl<sub>2</sub>). However, this tendency is completely overcompensated by increasing ion flux ( $\Gamma_+ = 2.9 \times 10^{15} - 4.8 \times 10^{15}$  cm<sup>-2</sup> s<sup>-1</sup> for 0–89% Cl<sub>2</sub>), so that the parameter  $\sqrt{M_i \epsilon_i} \Gamma_+$  also exhibits an increase in the range  $4.8 \times 10^{17} - 6.7 \times 10^{17}$  eV<sup>1/2</sup> cm<sup>-2</sup> s<sup>-1</sup> (Fig. 6a). A similar situation

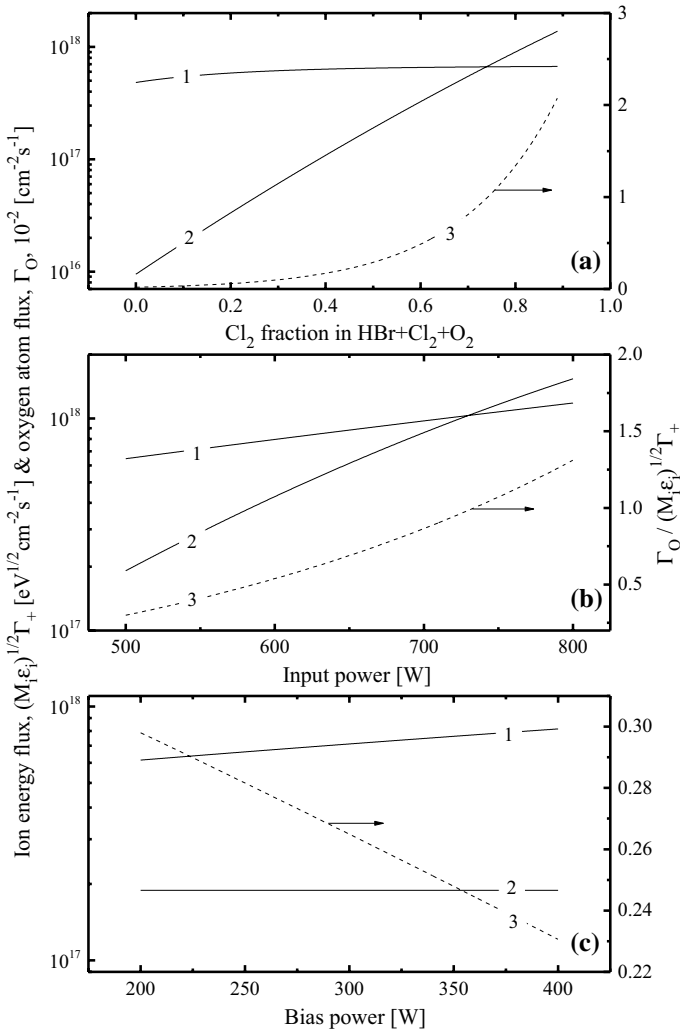


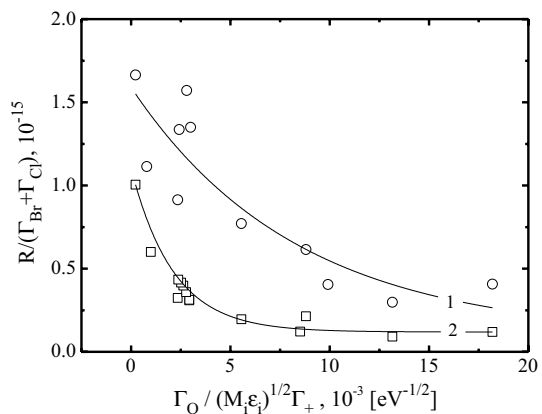
**Fig. 6** Ion energy flux (1), oxygen atom flux (2), and the parameter  $\Gamma_{\text{O}} / \sqrt{M_i \epsilon_i} \Gamma_+$  characterizing the impact of gas-phase plasma characteristics on effective reaction probability for Si and SiO<sub>2</sub> (3) as functions of Cl<sub>2</sub> fraction in a feed gas (a), input power (b), and bias power (c). The process conditions correspond to Fig. 1

occurs with variation in input power, where a change in  $\epsilon_i = 391\text{--}313$  eV corresponds to  $\sqrt{M_i \epsilon_i} \Gamma_+ = 6.4 \times 10^{17}\text{--}1.2 \times 10^{18}$   $\text{eV}^{1/2} \text{cm}^{-2} \text{s}^{-1}$  for 500–800 W (Fig. 6b). The variations in bias power influence the ion energy flux only through the changes in  $-U_{dc}$  and ion bombardment energy. Accordingly, an increase in  $W_{dc}$  from 200–400 W results in  $-U_{dc} = 375\text{--}567$  V (Fig. 2c) and  $\sqrt{M_i \epsilon_i} \Gamma_+ = 2.2 \times 10^{18}\text{--}6.2 \times 10^{18}$   $\text{eV} \text{cm}^{-2} \text{s}^{-1}$  (Fig. 6c). The data of Figs. 5 and 6 indicate opposite changes in  $\gamma_R$  and  $\sqrt{M_i \epsilon_i} \Gamma_+$  for the effects of  $y_{\text{Cl}_2}$  and input power, as well as a reasonable agreement between these parameters for the effect of bias power. Based on these findings, one can assume that the behaviors of  $\gamma_{R,\text{Si}}$  and  $\gamma_{R,\text{SiO}_2}$  are influenced by an additional factor connected with the chemistry of the neutral



species. Based on the results of Refs. [15, 17, 18], we suggest that this factor is the heterogeneous chemistry of O atoms. The mechanisms responsible for the negative impact of O atoms on effective reaction probabilities for both Si and SiO<sub>2</sub> may be connected with: (1) the formation of Si–O bonds that increases the reaction threshold for F atoms; and (2) the oxidation of reaction products into lower volatile SiBr<sub>x</sub>O<sub>y</sub> and SiCl<sub>x</sub>O<sub>y</sub> compounds. Obviously, the last mechanism decreases the desorption yield for reaction products and, thus, lowers the fraction of etched surfaces that are available for the adsorption of F atoms. Assuming that both ion energy flux and the O atoms flux have a nearly proportional relationship, but opposite influences on  $\gamma_R$ , one can roughly characterize their competitive effect by the  $\Gamma_O/\sqrt{M_i \epsilon_i} \Gamma_+$  ratio. From Fig. 6a, one can see that a change in  $y_{Cl_2}$  results in a much faster increase in  $\Gamma_O$  ( $1.1 \times 10^{14}$ – $1.2 \times 10^{16}$  cm<sup>-2</sup> s<sup>-1</sup>, or by ~110 times for 0–89% Cl<sub>2</sub>) compared with  $\sqrt{M_i \epsilon_i} \Gamma_+$ , and thus, results in a monotonically increasing  $\Gamma_O/\sqrt{M_i \epsilon_i} \Gamma_+$  ratio of Cl<sub>2</sub>-rich plasmas. Obviously, such a situation corresponds to decreasing  $\gamma_{R,Si}$  and  $\gamma_{R,SiO_2}$  values, as can be observed in Fig. 5a. Similarly, an increase in the O atom flux with increasing input power ( $\Gamma_O = 1.9 \times 10^{15}$ – $1.6 \times 10^{16}$  cm<sup>-2</sup> s<sup>-1</sup>, or by ~8.3 times for 500–800 W, see Fig. 6b) appears to be faster than the corresponding change in the ion energy flux. As a result, the  $\Gamma_O/\sqrt{M_i \epsilon_i} \Gamma_+$  ratio decreases by ~5 times, which is also reflected in the decreasing effective reaction probabilities for Si and SiO<sub>2</sub>. Finally, an increase in bias power increases the ion energy flux at  $\Gamma_O \approx \text{const}$ . Accordingly, one can obtain a decreasing  $\Gamma_O/\sqrt{M_i \epsilon_i} \Gamma_+$  ratio ( $3.1 \times 10^{-3}$ – $2.3 \times 10^{-3}$  for 200–400 W, see Fig. 6c) and increasing  $\gamma_{R,Si}$  and  $\gamma_{R,SiO_2}$ . Therefore, in all three cases, the change in effective reaction probability is in principal agreement with the  $\Gamma_O/\sqrt{M_i \epsilon_i} \Gamma_+$  ratio. In fact, this confirms the general reasonability of our assumption on the role of O atoms in both Si and SiO<sub>2</sub> etching processes in the HBr + Cl<sub>2</sub> + O<sub>2</sub> gas mixture. Furthermore, the data shown in Fig. 7 indicates that a correlation exists between the parameters  $R/(\Gamma_{Br} + \Gamma_{Cl})$  and  $\Gamma_O/\sqrt{M_i \epsilon_i} \Gamma_+$ . The shapes of the curves are quite close to those obtained in experiments for the correlations between Si and SiO<sub>2</sub> etching yields and the thickness of the deposited polymer film in the fluorocarbon gas plasmas [3–5, 35]. This probably means that the most realistic mechanism for the effect of oxygen on the effective reaction probabilities for Si and SiO<sub>2</sub> is connected with the formation of low-volatile SiBr<sub>x</sub>O<sub>y</sub> and SiCl<sub>x</sub>O<sub>y</sub> product layers, which reduces the permittivity of F atoms and ions on the etched surface. Finally, we would like to note that the etching rate of photoresist is as expected and always follows a change in  $\Gamma_O$ . The acceleration of the photoresist etching process with increasing  $W_{dc}$  under the condition of

**Fig. 7** The correlation between the parameters  $R/(\Gamma_{Br} + \Gamma_{Cl})$  and  $\Gamma_O/\sqrt{M_i \epsilon_i} \Gamma_+$  for Si (1) and SiO<sub>2</sub> (2). The shown points cover the full range of process parameters while the lines are to guide the eye only



$\Gamma_O \approx \text{const}$  may be reasonably associated with: (1) an increase in the polymer fragmentation rate by ion bombardment according to the change in  $\sqrt{M_i \epsilon_i} \Gamma_+$ ; and (2) the increase in surface temperature within the thin layer determined by the ion penetration depth. Obviously, all these intensify the chemical etching rate of photoresist by O atoms.

Certainly, one can understand that the proposed mechanism provides mainly a qualitative analysis of the Si and SiO<sub>2</sub> etching kinetics owing to the evident simplifications of primary assumptions. At the same time, the results of this work allow one to trace the relationships between input process conditions and the etching rates through bulk plasma characteristics (internal plasma parameters, kinetics of plasma active species) and the oxygen atom flux-sensitive reaction probability. Therefore, the given approach can be an effective tool for obtaining information on the etching process kinetics, as well as for etching process optimization.

## Conclusion

In this work, we investigated the Si and SiO<sub>2</sub> etching kinetics in the HBr + Cl<sub>2</sub> + O<sub>2</sub> inductively coupled plasma with variable HBr/Cl<sub>2</sub> mixing ratio, input power, and bias power. Furthermore, we attempted to determine the peculiarities of the etching mechanisms for both materials based on the relationships between the etching rates and gas-phase plasma characteristics (plasma parameters, densities, and the fluxes of active species). For this purpose, we employed a combination of plasma diagnostics by Langmuir probes and 0-dimensional plasma modeling. It was found that the variations in the HBr/Cl<sub>2</sub> mixing ratio and input power cause similar increasing tendencies for ion energy flux and halogen atom flux, but result in different changes for both Si and SiO<sub>2</sub> etching rates. It was shown that the influence of input process parameters on the Si and SiO<sub>2</sub> etching kinetics may be adequately described in terms of the oxygen atom flux-sensitive reaction probability, which directly correlates with the oxygen atom flux/ion energy flux ratio. The most realistic mechanism for the effect of oxygen on the effective reaction probabilities of Si and SiO<sub>2</sub> may be connected with the formation of low-volatile SiBr<sub>x</sub>O<sub>y</sub> and SiCl<sub>x</sub>O<sub>y</sub> product layers, which reduces the permittivity of F atoms and ions on the etched surface.

**Acknowledgements** This research was supported by MOTIE [Ministry of Trade, Industry & Energy (No. 10052890)] and the KSRC (Korea Semiconductor Research Consortium) support program for the development of future semiconductor devices.

## References

1. Wolf S, Tauber RN (2000) Silicon processing for the VLSI Era. Volume 1. Process technology. Lattice Press, New York
2. Rooth JR (1995) Industrial plasma engineering. IOP Publishing Ltd., Philadelphia
3. Sugano T (1990) Applications of plasma processes to VLSI technology. John Wiley & Sons, University of Michigan, New York
4. Sze SM (1988) VLSI technology. McGraw-Hill, New York
5. Coburn JW (1982) Plasma etching and reactive ion etching. AVS monograph series. American Institute of Physics (AIP), New York
6. Jansen H, Gardeniers H, deBoer M, Elwenspoek M, Fluitman J (1996) A survey on the reactive ion etching of silicon in microtechnology. *J Micromech Microeng* 6(1):14–29
7. Nojiri K (2015) Dry etching technology for semiconductors. Springer, Berlin

8. Vitale SA, Chae H, Sawin HH (2001) Silicon etching yields in  $F_2$ ,  $Cl_2$ ,  $Br_2$ , and  $HBr$  high density plasmas. *J Vac Sci Technol, A* 19(5):2197–2206
9. Cheng CC, Guinn KV, Herman IP, Donnelly VM (1995) Competitive halogenation of silicon surfaces in  $HBr/Cl_2$  plasmas studied ray photoelectron-spectroscopy and in situ, real-time, pulsed laser-induced thermal-desorption. *J Vac Sci Technol, A* 13(4):1970–1976
10. Cunge G, Kogelschatz M, Joubert O, Sadeghi N (2005) Plasma-wall interactions during silicon etching processes in high-density  $HBr/Cl_2/O_2$  plasmas. *Plasma Sources Sci Technol* 14(2):S42–S52
11. Tokashiki K, Ikawa E, Hashimoto T, Kikkawa T, Teraoka Y, Nishiyama I (1991) Influence of halogen plasma atmosphere on  $SiO_2$  etching characteristics. *Jpn J Appl Phys* 1 30(11b):3174–3177
12. Yeom GY, Ono Y, Yamaguchi T (1992) Polysilicon etchback plasma process using  $HBr$ ,  $Cl_2$ , and  $SF_6$  gas-mixtures for deep-trench isolation. *J Electrochem Soc* 139(2):575–579
13. Chuang MC, Coburn JW (1990) Molecular-beam study of gas-surface chemistry in the ion-assisted etching of silicon with atomic and molecular-hydrogen and chlorine. *J Vac Sci Technol, A* 8(3):1969–1976
14. Donnelly VM, Klemens FP, Sorsch TW, Timp GL, Baumann FH (1999) Oxidation of Si beneath thin  $SiO_2$  layers during exposure to  $HBr/O_2$  plasmas, investigated by vacuum transfer x-ray photoelectron spectroscopy. *Appl Phys Lett* 74(9):1260–1262
15. Kim DK, Kim YK, Lee H (2007) A study of the role of  $HBr$  and oxygen on the etch selectivity and the post-etch profile in a polysilicon/oxide etch using  $HBr/O_2$  based high density plasma for advanced DRAMs. *Mat Sci Semiconduct Proc* 10(1):41–48
16. Belen RJ, Gomez S, Kiehlauch M, Aydil ES (2006) Feature scale model of Si etching in  $SF_6/O_2/HBr$  plasma and comparison with experiments. *J Vac Sci Technol, A* 24(2):350–361
17. Mcnevin SC (1990) Radio-frequency plasma-etching of  $Si/SiO_2$  by  $Cl_2/O_2$ —improvements resulting from the time modulation of the processing gases. *J Vac Sci Technol, B* 8(6):1185–1191
18. Tinck S, Boullart W, Bogaerts A (2011) Modeling  $Cl_2/O_2/Ar$  inductively coupled plasmas used for silicon etching: effects of  $SiO_2$  chamber wall coating. *Plasma Sources Sci Technol* 20:045012
19. Efremov A, Kim Y, Lee HW, Kwon KH (2011) A comparative study of  $HBr-Ar$  and  $HBr-Cl_2$  plasma chemistries for dry etch applications. *Plasma Chem Plasma Proc* 31(2):259–271
20. Efremov A, Lee J, Kwon KH (2017) A comparative study of  $CF_4$ ,  $Cl_2$  and  $HBr + Ar$  inductively coupled plasmas for dry etching applications. *Thin Solid Films* 629:39
21. Bazin A, Pargon E, Mellhaoui X, Perret D, Mortini B, Joubert O (2008) Advances in resist materials and processing technology XXV. In: Henderson CL (ed) *Proceedings of the SPIE* 6923:692337
22. Pargon E, Menguelti K, Martin M, Bazin A, Chaix-Pluchery O, Sourd C, Derrough S, Lill T, Joubert O (2009) Mechanisms involved in  $HBr$  and  $Ar$  cure plasma treatments applied to 193 nm photoresists. *J Appl Phys* 105(9)
23. Bestwick TD, Oehrelein GS (1990) Reactive ion etching of silicon using bromine containing plasmas. *J Vac Sci Technol, A* 8(3):1696–1701
24. Jin WD, Vitale SA, Sawin HH (2002) Plasma-surface kinetics and simulation of feature profile evolution in  $Cl_2 + HBr$  etching of polysilicon. *J Vac Sci Technol, A* 20(6):2106–2114
25. Lee HW, Kim M, Min NK, Efremov A, Lee CW, Kwon KH (2008) Etching characteristics and mechanism of  $InP$  in inductively coupled  $HBr/Ar$  plasma. *Jpn J Appl Phys* 47(8):6917–6922
26. Johnson EO, Malter L (1950) a floating double probe method for measurements in gas discharges. *Phys Rev* 80(1):58–68
27. Sugavara M (1998) *Plasma etching: fundamentals and applications*. Oxford University Press, New York
28. Efremov A, Min NK, Choi BG, Baek KH, Kwon KH (2008) Model-based analysis of plasma parameters and active species kinetics in  $Cl_2/X$  ( $X = Ar, He, N_2$ ) inductively coupled plasmas. *J Electrochem Soc* 155(12):D777–D782
29. Kwon KH, Efremov A, Kim M, Min NK, Jeong J, Kim K (2010) A model-based analysis of plasma parameters and composition in  $HBr/X$  ( $X = Ar, He, N_2$ ) inductively coupled plasmas. *J Electrochem Soc* 157(5):H574–H579
30. Lee BJ, Lee BJ, Efremov A, Yang JW, Kwon KH (2016) Etching characteristics and mechanisms of  $MoS_2$  2D crystals in  $O_2/Ar$  inductively coupled plasma. *J Nanosci Nanotechnol* 16(11):11201–11209
31. Efremov AM, Kim GH, Kim JG, Bogomolov AV, Kim CI (2007) On the applicability of self-consistent global model for the characterization of  $Cl_2/Ar$  inductively coupled plasma. *Microelectron Eng* 84:136–143
32. Hsu CC, Nierode MA, Coburn JW, Graves DB (2006) Comparison of model and experiment for  $Ar$ ,  $Ar/O_2$  and  $Ar/O_2/Cl_2$  inductively coupled plasmas. *J Phys D Appl Phys* 39(15):3272–3284
33. Lee C, Lieberman MA (1995) Global-model of  $Ar$ ,  $O_2$ ,  $Cl_2$ , and  $Ar/O_2$  high-density plasma discharges. *J Vac Sci Technol, A* 13(2):368–380

34. Kwon KH, Efremov A, Yun SJ, Chun I, Kim K (2014) Dry etching characteristics of Mo and Al<sub>2</sub>O<sub>3</sub> films in O<sub>2</sub>/Cl<sub>2</sub>/Ar inductively coupled plasmas. *Thin Solid Films* 552:105–110
35. Lieberman MA, Lichtenberg AJ (1994) Principles of plasma discharges and materials processing. Wiley, New York
36. Itikawa Y, Mason N (2005) Cross sections for electron collisions with water molecules. *J Phys Chem Ref Data* 34(1):1–22
37. Morgan WL (1992) A critical-evaluation of low-energy electron-impact cross-sections for plasma processing modeling. I: Cl<sub>2</sub>, F<sub>2</sub>, and HCL. *Plasma Chem Plasma P* 12(4):449–476
38. NIST Chemical Kinetics Database <http://kinetics.nist.gov/kinetics/index.jsp>. Accessed 1 Nov 2018
39. Corr CS, Despiau-Pujo E, Chabert P, Graham WG, Marro FG, Graves DB (2008) Comparison between fluid simulations and experiments in inductively coupled argon/chlorine plasmas. *J Phys D Appl Phys* 41:(18)
40. Curley GA, Gatilova L, Guilet S, Bouchoule S, Gogna GS, Sirse N, Karkari S, Booth JP (2010) Surface loss rates of H and Cl radicals in an inductively coupled plasma etcher derived from time-resolved electron density and optical emission measurements. *J Vac Sci Technol, A* 28(2):360–372
41. Kota GP, Coburn JW, Graves DB (1999) Heterogeneous recombination of atomic bromine and fluorine. *J Vac Sci Technol A* 17(1):282–290
42. Serdyuk NK, Gutorov VV, Panfilov VN (1981) Studies of the reactions of Br(<sup>2</sup>P<sub>3/2</sub>) and Br(<sup>2</sup>P<sub>1/2</sub>) with SiH<sub>4</sub>. *React Kinet Catal L* 16(4):393–397
43. Wood BJ, Wise H (1961) Kinetics of hydrogen atom recombination on surfaces. *J Phys Chem-US* 65(11):1976
44. Ashida S, Lieberman MA (1997) Spatially averaged (global) model of time modulated high density chlorine plasmas. *Jpn J Appl Phys* 36(2):854–861
45. Jang H, Efremov A, Kim D, Kang S, Yun SJ, Kwon KH (2012) Etching characteristics and mechanisms of TiO<sub>2</sub> thin films in HBr/Ar and Cl<sub>2</sub>/Ar inductively-coupled plasmas. *Plasma Chem Plasma Proc* 32(2):333–342
46. Gray DC, Tepermeister I, Sawin HH (1993) Phenomenological modeling of ion-enhanced surface kinetics in fluorine-based plasma-etching. *J Vac Sci Technol, B* 11(4):1243–1257
47. Lee C, Graves DB, Lieberman MA (1996) Role of etch products in polysilicon etching in a high-density chlorine discharge. *Plasma Chem Plasma Proc* 16(1):99–120
48. Efremov AM, Kim DP, Kim CI (2004) Simple model for ion-assisted etching using Cl<sub>2</sub>-Ar inductively coupled plasma: effect of gas mixing ratio. *IEEE Trans Plasma Sci* 32(3):1344–1351
49. Ito T, Karahashi K, Kang S-Y, Hamaguchi S (2010) Evaluation of Si etching yields by Cl<sup>+</sup>, Br<sup>+</sup>, and HBr<sup>+</sup> ion irradiation. *J Phys: Conf Ser* 232:012021
50. Lide DR (1998–1999) Handbook of chemistry and physics. CRC Press, New York
51. Chapman B (1980) Glow discharge processes: sputtering and plasma etching. Wiley, New York